



**HAL**  
open science

## Directional crystallization of C8-BTBT-C8 thin films in a temperature gradient

Guillaume Schweicher, Guangfeng Liu, Pierre Fastré, Roland Resel, Mamatimin Abbas, Guillaume Wantz, Yves Henri Geerts

► **To cite this version:**

Guillaume Schweicher, Guangfeng Liu, Pierre Fastré, Roland Resel, Mamatimin Abbas, et al.. Directional crystallization of C8-BTBT-C8 thin films in a temperature gradient. *Materials Chemistry Frontiers*, 2021, 5 (1), pp.249-258. 10.1039/D0QM00472C . hal-03434752

**HAL Id: hal-03434752**

**<https://hal.science/hal-03434752>**

Submitted on 23 Nov 2021

**HAL** is a multi-disciplinary open access archive for the deposit and dissemination of scientific research documents, whether they are published or not. The documents may come from teaching and research institutions in France or abroad, or from public or private research centers.

L'archive ouverte pluridisciplinaire **HAL**, est destinée au dépôt et à la diffusion de documents scientifiques de niveau recherche, publiés ou non, émanant des établissements d'enseignement et de recherche français ou étrangers, des laboratoires publics ou privés.

## ARTICLE

## Directional Crystallization of C8-BTBT-C8 Thin Films in a Temperature Gradient

Guillaume Schweicher,<sup>a</sup> Guangfeng Liu,<sup>a\*</sup> Pierre Fastré,<sup>a</sup> Roland Resel,<sup>b</sup> Mamatimin Abbas,<sup>c</sup> Guillaume Wantz<sup>c</sup> and Yves Henri Geerts<sup>a,d</sup>

Received 00th January 20xx,  
Accepted 00th January 20xx

DOI: 10.1039/x0xx00000x

A directional crystallization of compound 2,7-dioctyl[1]benzothieno[3,2-b][1]benzothiophene (C8-BTBT-C8) based on a temperature gradient approach has been used as a post-deposition process to control the crystalline morphology of thin films. C8-BTBT-C8 films of arbitrary thicknesses have been fabricated by spin-coating and subjected to the directional crystallization process. Dewetting is prevented by the liquid crystal phase of C8-BTBT-C8, allowing the formation of flat and rather uniform thin films with large crystalline domains. Spin-coating concentration, gradient magnitude, and cooling rate have been varied to explore a large set of crystallization conditions and to correlate them with thin film morphology. The latter has been characterized by a combined use of optical profilometer, polarized optical microscopy, X-ray reflectometry, and X-ray diffraction measurements. The characterization results put forward the roughness and crystalline order of thin films are improved after the temperature gradient treatments: **1.** high cooling rates treatments ( $\geq 9\text{ }^{\circ}\text{C}\cdot\text{min}^{-1}$ ) significantly reduce the roughness of high thickness films, leading good continuity and uniform of the films; **2.** dendritic growth dominates not only the films with low thickness but also films with high thickness treated under low cooling rates ( $< 9\text{ }^{\circ}\text{C}\cdot\text{min}^{-1}$ ); **3.** the out-of-plane order and the in-plane alignment of the crystallites are also remarkably enhanced by the temperature gradient treatments.

### Introduction

In the last three decades, thin-film of organic semiconductors (OSCs) have attracted considerable attention, because they are key components for constructing the next-generation light-weight, stretchable and wearable optoelectronic organic devices.<sup>1-7</sup> The control of thickness, roughness, and crystalline morphology at different length-scales and over large area are crucial for the performances of OSCs.<sup>8-10</sup> Crystalline morphology is defined here as comprising crystal shape, crystal size, crystal orientation, crystal alignment, less ordered regions, defects, polymorphs, and grain boundaries. The fabrication of high-quality, large-scale ( $> 1\text{ cm}^2$ ) single crystalline thin-film of OSCs remains challenging.<sup>11-14</sup> Thin films of OSCs are fabricated either by vapor deposition, solution processing, or from melt, each method bearing its own advantages and disadvantages. Vapor deposition, which is only applicable to small molecules, allows the reproducible obtaining of thin films

with controlled thickness and roughness. The orientation of the molecules versus a substrate, which is governed by the anisotropy of surface tension of the different crystallographic faces, is generally spontaneously achieved. Grain size and grain boundary width are controllable by pressure, deposition rate and temperature conditions. However, the alignment of crystals along a specific in plane direction generally requires preliminary substrate patterning.<sup>13, 15, 16</sup> A plethora of solution deposition techniques, such as for example drop-casting, spin-coating, inkjet printing, dip coating, blade coating, zone casting, and edge casting, have been developed for both small molecules and polymers.<sup>11, 16</sup> They evidently require a sufficient solubility in solvents. Drop-casting allows nearly no control of either thickness, roughness, or morphology. Spin-coating is a widely applicable method for obtaining films of tailored thickness and roughness, but with poor control of crystalline morphology. Inkjet printing has the advantage of easy patterning of thin films on the micron scale.<sup>17</sup> Dip coating, blade coating, zone casting, and edge casting are directional methods with good control of thickness, roughness, and crystalline morphology, including some alignment.<sup>14, 15, 18</sup> Over the years, shearing has emerged as one of the best technique for thin film fabrication.<sup>19-21</sup> Thin rather uniform aligned films are achievable and even some new polymorphs have been obtained.<sup>19,21</sup> Through optimization of solvent evaporation conditions, wafer scale single crystals as thin as one molecular layer have been obtained by the shearing technique.<sup>22</sup> A less visited approach is the production of crystalline thin films from the melt.<sup>23-26</sup> In the past few years, our group has investigated the directional crystallization of organic

<sup>a</sup> Laboratoire de chimie des polymères, Faculté des Sciences, Université Libre de Bruxelles (ULB), CP 206/01, Boulevard du Triomphe, 1050, Brussels, Belgium

<sup>b</sup> Institute of Solid State Physics, Graz University of Technology, Petersgasse 16, 8010 Graz, Austria.

<sup>c</sup> Université de Bordeaux, IMS, CNRS, UMR-5218, Bordeaux INP, ENSCBP, 33405 Talence, France

<sup>d</sup> International Solvay Institutes of Physics and Chemistry, ULB, CP 231, Boulevard du Triomphe, 1050 Brussels, Belgium

E-mail: gliu@ulb.ac.be

Electronic Supplementary Information (ESI) available: calibration of the magnitude of the temperature gradient set-up, TGA, 3D views of optical profilometer, XRR, sXRD, POM pictures and Tables. See DOI: 10.1039/x0xx00000x

solids starting from their melt by using a temperature gradient ( $\nabla T$ ) (Figure 1).<sup>27-30</sup> This technique, also known as directional crystallization or solidification, is essentially the adaptation of the method of Percy Bridgman to thin films of molecular compounds using the set-up invented by Kenneth Jackson.<sup>31</sup> Although this technique has commonly been used for the study of organic compounds such as for example n-alkanes and m-nitroaniline,<sup>32-36</sup> it has not widely been studied to control the crystalline morphology of OSC thin films. This technique presents several advantages: i) nucleation and growth processes are decoupled, ii) growth occurs preferentially through some selected crystallographic faces, iii) uniaxial alignment takes place, iv) the number of molecules entering the crystal phase per unit time and through some crystallographic faces is externally controllable.<sup>27-30</sup>

Up to now, the temperature gradient method has been applied to rather thick films ( $\mu\text{m}$  thick) sandwiched between two glass slides to avoid the unwanted dewetting of the melt state.<sup>37</sup> As a consequence, film thickness could hardly be controlled unless for OSCs exhibiting a smectic phase before the isotropization temperature ( $T_{\text{iso}}$ ). Indeed, smectic phases are less prone to dewetting and tend to spread on substrates, allowing direct processing in a thermal gradient from a non-sandwiched thin film as we will describe further now.<sup>38, 39</sup> Firstly, a thin film of arbitrary thickness is conventionally fabricated by spin-coating. Then, the gradient method exploiting the crystal to smectic transition is used as a post-deposition processing method to tailor crystalline morphology. 2,7-dioctyl[1]benzothieno[3,2-*b*][1]benzothiophene, abbreviated C8-BTBT-C8, which is a largely studied OSC, forms a smectic A (SmA) phase from 110 to 126°C and qualifies as adequate molecular system for such study.<sup>26, 40-42</sup> The goal of this work is to investigate the crystalline morphology of thin films of C8-BTBT-C8 as a function of the directional crystallization conditions.

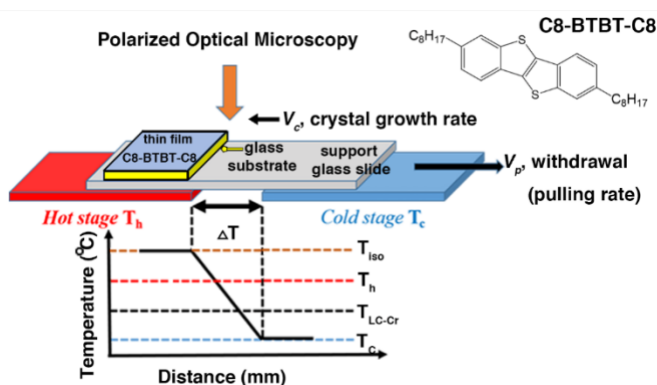


**Fig.1** Schematic drawing of the  $\nabla T$  set-up.  $T_{\text{iso}}$  and  $T_{\text{LC-cr}}$  are the isotropization and the liquid-crystal to crystal phase transition temperatures, respectively.  $T_{\text{h}}$  and  $T_{\text{c}}$  are the temperatures of the hot and cold stage.  $\Delta T$  is the temperature difference between the hot and cold stage.  $V_{\text{p}}$  and  $V_{\text{c}}$  are the lateral pulling rate and the crystal growth rate of the sample. The sample is constituted of a glass substrate covered by a thin film of C8-BTBT-C8. Inset: the molecular structure of C8-BTBT-C8.

## Experimental

**1. Materials.** C8-BTBT-C8 and 2,7-didodecyl[1]benzothieno[3,2-*b*][1]benzothiophene, abbreviated C12-BTBT-C12, have been synthesized according to literature.<sup>40</sup> Before using, these two compounds were purified by sublimation in a tube furnace. HPLC-grade (>99.8%, Sigma-Aldrich) toluene solvent was used without further purification. 15 mm  $\times$  10 mm  $\times$  0.7 mm sized glass substrates (D 263 Borosilicate thin glass from Präzisions Glas & Optik GmbH, Germany) were used for the experiments. They were sonicated for 10 minutes in deionized water and acetone, then blown dry with nitrogen and exposed 30 minutes to an ultraviolet-ozone (Procleaner plus; Bioforce Nanosciences) treatment before the experiments.

**2. Differential scanning calorimetry (DSC) and thermogravimetric analysis (TGA).** DSC was performed at 10 °C.min<sup>-1</sup> under a dry nitrogen gas atmosphere in a Perkin Elmer Diamond 6 instrument (temperature range 30-150 °C). TGA measurement was performed in a Perkin Elmer Pyris 6 TGA. Powder sample underwent a linear ramp of increasing temperature up to 600 °C at a rate of 10 °C.min<sup>-1</sup> in an inert atmosphere of nitrogen.

**3. Polarized Optical Microscopy (POM).** The  $\nabla T$  hot stage is mounted on a POM (Nikon Eclipse 80i) allowing in situ observations. The pictures of the thin films were recorded before and after the thermal gradient treatment by a Carl Zeiss AXiO Imager. A1 POM.

**4. Temperature gradient apparatus.** The set-up shown in Figure 1, consists of a Linkam GS350 system presenting two individual heating stages separated by a gap. The distance (gap) between the two stages where the thermal gradient will be generated is of 2 mm. During the  $\nabla T$  experiments, the hot stage is set at a temperature  $T_{\text{h}}$ , situated between the isotropization temperature of the material, C8-BTBT-C8 ( $T_{\text{iso}}$ ), and the LC to crystal transformation temperature ( $T_{\text{LC-cr}}$ ); while the cold stage is maintained at a temperature  $T_{\text{c}}$ , below  $T_{\text{LC-cr}}$  of C8-BTBT-C8.  $T_{\text{iso}}$  and  $T_{\text{LC-cr}}$  temperature values were evaluated by DSC. The system is covered by a hermetic lid so that the system is thermally independent from the laboratory environment.

**5. C8-BTBT-C8 thin films fabrication by the  $\nabla T$  method.** C8-BTBT-C8 thin films were initially prepared by spin-coating (Specialty Coating Systems Model P6700 Series spin-coater) with different solution concentrations (2.3 mg.ml<sup>-1</sup>, 5.4 mg.ml<sup>-1</sup>, 10.5 mg.ml<sup>-1</sup>, 13.5 mg.ml<sup>-1</sup>, and 20 mg.ml<sup>-1</sup>; solvent: toluene), on pre-cleaned 15 mm  $\times$  10 mm  $\times$  0.7 mm thin glass substrates. The spin-coating parameters are as following: 150  $\mu\text{L}$  solution, 150 RPM (5s, the first step), 1500 RPM (5s, the second step), and 3000 RPM (30s, final step). The thickness of thin films was measured by X-ray reflectivity (XRR). Thin films of C8-BTBT-C8 were then processed in the  $\nabla T$ . The  $\nabla T$  treatments for ten spin-coated samples, produced using a 20 mg.ml<sup>-1</sup> concentration, were carried out using two  $T_{\text{h}} - T_{\text{c}}$  couples: 1) 120 °C - 90 °C and 2) 120 °C - 60 °C, and five different pulling rates ( $v_{\text{p}}$ : 1  $\mu\text{m.s}^{-1}$ , 5  $\mu\text{m.s}^{-1}$ , 10  $\mu\text{m.s}^{-1}$ , 25  $\mu\text{m.s}^{-1}$  and 50  $\mu\text{m.s}^{-1}$ ) respectively, see Table 1 for full conditions.

**6. X-ray measurements. X-ray reflectometry (XRR):** XRR curves of the C8-BTBT-C8 thin films were collected on a Bruker D8 Advance diffractometer using Cu K $\alpha$  radiation ( $\lambda = 1.5418 \text{ \AA}$ ) at room temperature.  $2\theta$  ranges between 0.4° and 3.8° with an angular resolution of 0.005° per step and a typical counting time

of 5s, using a  $\theta/\theta$  (specular) reflection geometry. XRR curves are presented as the scattering intensity versus the scatter vector,  $q_z$  ( $\text{\AA}^{-1}$ ), using Equation 1:  $q = 4\pi \times \sin\theta/\lambda$ , where  $\lambda = 1.5418 \text{ \AA}$ . The thickness of the thin films can be evaluated by the angular separation between two maxima (constructive interference) or minima (destructive interference) of consecutive fringes using Equation 2:  $n = 2\pi/(q_1 - q_2)$ , where  $n$  is the thickness of thin film;  $q_i$  is the momentum transfer of an extremum. The XRR curves show a total external reflection plateau up to  $q_z = 0.34 \text{ nm}^{-1}$  (on glass substrates) providing information on the critical angle. The value of the total reflection critical angle is similar to the one achieved in our previous XRR studies of spin-coated thin films of C8-BTBT-C8 on Si-wafers covered with a 150 nm thermally grown oxide layer ( $q_z = 0.31 \text{ nm}^{-1}$ ).<sup>38</sup> The FWHM (full width at half the maximum of a diffraction peak) of the (002) Bragg peak ( $q_z$  around  $4.34 \text{ nm}^{-1}$ ) was determined. The coherence length,  $L_c$  (perpendicular to the substrate surface in this case, that is, the vertical crystallite size), was estimated using the Scherrer equation<sup>43</sup> (Equation 3:  $L_c = 2\pi/\Delta q$ ,  $\Delta q$  is the FWHM).

**Specular X-ray diffraction (sXRD):** sXRD pattern of C8-BTBT-C8 powder sample was collected on a Bruker D8 Advance diffractometer using Cu K $\alpha$  radiation ( $\lambda = 1.5418 \text{ \AA}$ ) at room temperature, in the  $2\theta$  range between  $2^\circ$  and  $40^\circ$  with an increment of  $0.02^\circ$  per step and a counting time of 0.5 s per step at room temperature. sXRD pattern of the LC phase was collected on a Bruker D8 Advance diffractometer using Cu K $\alpha$  radiation ( $\lambda = 1.5418 \text{ \AA}$ ) and equipped with a MRI (Material Research Instruments) heating stage for high temperature measurements, using similar parameters except a  $2\theta$  range between  $2^\circ$  and  $30^\circ$ . sXRD patterns for thin films were collected on a Rigaku Ultima IV diffractometer using Cu K $\alpha$  radiation ( $\lambda = 1.5418 \text{ \AA}$ ), in the  $2\theta$  range between  $2^\circ$  and  $10^\circ$  with an increment of  $0.02^\circ$  per step and a counting time of 0.15 s per step at room temperature.

**In-plane GIXD:** in-plane grazing incidence XRD measurements were performed on a Rigaku Ultima IV diffractometer using Cu K $\alpha$  radiation ( $\lambda = 1.5418 \text{ \AA}$ ). An in-plane  $2\theta_\chi/\phi$  scan is a technique for measuring lattice planes normal to the surface of a thin film. The direction of the scatter vector is kept constant. A grazing-incident X-ray beam is employed in a  $2\theta_\chi/\phi$  scan in-plane XRD measurement so that the incident X-ray beam travels a long distance inside the thin film, and thus high diffraction intensities from the film could be obtained. Meanwhile, the angle of the incident X-ray beam can be controlled independently on the sample rotation angle ( $\phi$ ) and the position of the detector ( $2\theta_\chi$ ) in the geometry of a  $2\theta_\chi/\phi$  scan.  $2\theta_\chi/\phi$  scans for thin films were carried out in the  $2\theta_\chi$  range between  $5^\circ$  and  $50^\circ$  with a sampling of  $0.02^\circ$  per step and a speed of  $0.08^\circ \text{ min}^{-1}$  at room temperature. The beam incident angle  $\alpha_i$  has been kept at  $0.18^\circ$ .

**XRD pole figures:** pole-figure measurement is an XRD technique where the diffraction angle ( $2\theta$ ) is fixed and the diffracted intensity is collected by varying the tilt angle from the sample surface normal direction ( $\Psi$ ) and the rotation angle around the sample surface normal ( $\phi$ ). The obtained diffracted intensity data can be plotted as a function of the tilt angle and rotation angle to quantitatively evaluate the orientation texture of the sample. Pole figures for the different C8-BTBT-C8 thin film

samples were measured on a PHILIPS X'Pert system equipped with an ATC3 cradle using Cr K $\alpha$  radiation ( $\lambda = 2.291 \text{ \AA}$ ) and a graphite secondary monochromator. The schematic representation of the pole-figure measurement geometry is shown in Figure S13. Pole figures were plotted using the software STEREOPOLE.<sup>44</sup>

**7. Optical profilometer.** The surface morphology study of the C8-BTBT-C8 thin films before and after the VT treatment was carried out using an optical profilometer (Veeco NT9080) by a phase shifting interferometry (PSI) mode. Each image was analysed by the software Vision 4.3 to get the 3D surface morphology and surface roughness statistics (Ra). Ra is the arithmetical mean deviation of the assessed profile.

$$Ra = \frac{1}{A} \iint_A |z(x, y)| dx dy$$

Equation 4: where A is the area of the defined range,  $|z(x, y)|$  is the distance between a point (x,y) in the plane and the center plane.

**8. Crystal morphology calculation.** The crystal morphology of C8-BTBT-C8 was predicted using the software Mercury 3.10.3 based on the Bravais-Friedel-Donnay-Harker (BFDH) method.<sup>45-47</sup>

**9. Calibration of the magnitude of the temperature gradient setup ( $G_{exp}$ ).** Previous work has shown that the effective magnitude of temperature gradient ( $G_{exp}$ ) that takes place between the hot and cold zones is less than the magnitude simply calculated by the equation as  $G = (T_h - T_c)/x$ , where  $x = 2.0 \text{ mm}$  is the gap between the hot and cold stages.<sup>27-30</sup> The calibration of the VT setup has been carried out as previously reported<sup>30</sup> and is detailed in supporting information (Table S1 and Figure S1).  $G_{1exp} \approx 6$  and  $G_{2exp} \approx 11^\circ \text{C} \cdot \text{mm}^{-1}$  for  $T_h - T_c$  couples  $120^\circ \text{C} - 90^\circ \text{C}$  and  $120^\circ \text{C} - 60^\circ \text{C}$ , respectively.

## Results and discussion

### 1. Crystal structure and thermotropic behaviour of C8-BTBT-C8.

The crystal structure of C8-BTBT-C8, first reported by Takimiya *et al.* from single crystal X-ray diffraction measurements performed at 293 K, belongs to a monoclinic system, with a space group  $P2_1/a$  and unit cell parameters  $a = 5.907 \text{ \AA}$ ,  $b = 7.890 \text{ \AA}$ ,  $c = 29.086 \text{ \AA}$ , and  $\beta = 91.94^\circ$ .<sup>40</sup> The crystal morphology of C8-BTBT-C8, shown in Figure 2a, presents a lamellar hexagonal shape with edge-on upstanding molecules on the main face (001). The thermal stability of C8-BTBT-C8 is higher than  $300^\circ \text{C}$  (onset Temperature  $334^\circ \text{C}$ , shown in the TGA curve in Figure S2). The Cr-to-LC and LC-to-Cr phase transitions are reproducibly observed in the DSC curves (Figure 2b), showing a liquid crystal phase from  $108.9^\circ \text{C}$  to  $125^\circ \text{C}$  upon heating. The fan shaped features visible in the POM image at  $124^\circ \text{C}$  (Figure 2c) combined to the only two diffraction peaks visible in the sXRD pattern recorded at  $120^\circ \text{C}$  (Figure 2d) confirms the high temperature SmA phase of C8-BTBT-C8, in excellent agreement with previous data.<sup>38,40</sup>

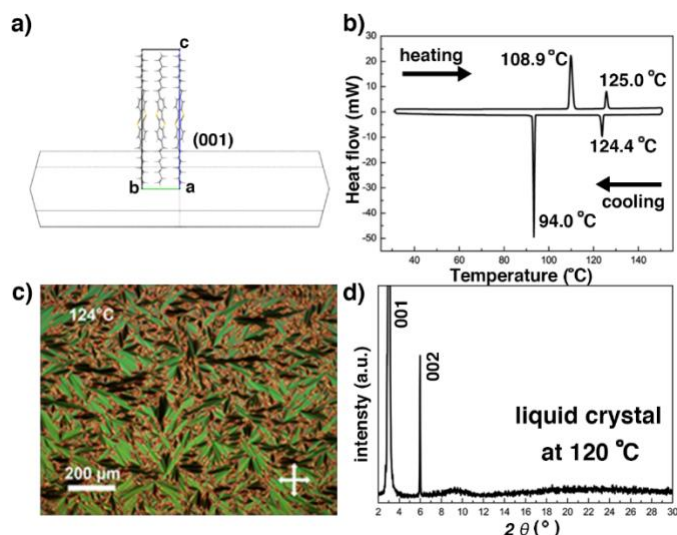


**Fig.2** (a) Predicted crystal morphology of C8-BTBT-C8 based on the BFDH method. (b) DSC trace of C8-BTBT-C8. (c) POM picture of the fan shaped texture of the SmA liquid crystal phase of C8-BTBT-C8 recorded at 124 °C. (d) sXRD pattern of the SmA phase recorded at 120 °C.

## 2. Crystallization of C8-BTBT-C8 thin films in $\nabla T$ using the LC to Cr transition.

### 2.1 Crystallization conditions.

First, thin films of C8-BTBT-C8 were prepared on borosilicate glass substrates by spin-coating from toluene solutions, using five different concentrations: 2.3 mg.ml<sup>-1</sup>, 5.4 mg.ml<sup>-1</sup>, 10.5 mg.ml<sup>-1</sup>, 13.5 mg.ml<sup>-1</sup> and 20 mg.ml<sup>-1</sup>. These films, numbered as samples **1-5**, serve as comparison point with samples **6-19** processed in thermal gradient, see Table 1. Note that borosilicate glass exhibits a higher thermal conductivity,  $\lambda = 0.926 \text{ Wm}^{-1}\text{K}^{-1}$  than the one of C8-BTBT-C8 along the *a* and *b* directions,  $\lambda \approx 0.18 \text{ Wm}^{-1}\text{K}^{-1}$ .<sup>48</sup> Moreover, C8-BTBT-C8 films are much thinner than glass slides. These two conditions ensure a rapid local thermalization of C8-BTBT-C8 films with their environment. Crystallization of C8-BTBT-C8 occurred in films **1-5** upon solvent evaporation during spin-coating with not much control (*vide infra*). Second, films of increasing thickness have been subjected to crystallization in the same  $\nabla T$  conditions (films **6** to **10**). Third, the thickest films, spin-coated at 20 mg.ml<sup>-1</sup>, have been crystallized in various  $\nabla T$  conditions, i.e. with  $1 \leq V_p \leq 50 \text{ }\mu\text{m.s}^{-1}$  and with using  $G_{exp} \approx 6$  and  $11 \text{ }^\circ\text{C.mm}^{-1}$ , to explore a large set of experimental conditions (films **10** to **19**). The cooling rate at the growth front has been varied by nearly two order of magnitudes, i.e. ranging from 0.36 to  $33 \text{ }^\circ\text{C.min}^{-1}$  (Table 1).

**Table 1.**  $\nabla T$  crystallization conditions for the C8-BTBT-C8 thin films.

Films No.	Concentration mg.ml <sup>-1</sup>	$T_h$ °C	$T_c$ °C	$V_p$ $\mu\text{m.s}^{-1}$	$G_{exp}$ °C.mm <sup>-1</sup>	$C_{exp}^*$ °C.min <sup>-1</sup>
6	2.3	120	90	25	6	9
7	5.4	120	90	25	6	9
8	10.5	120	90	25	6	9
9	13.5	120	90	25	6	9
10	20	120	90	25	6	9
11	20	120	90	1	6	0.36
12	20	120	60	1	11	0.66
13	20	120	90	5	6	1.8
14	20	120	60	5	11	3.3
15	20	120	90	10	6	3.6
16	20	120	60	10	11	6.6
17	20	120	60	25	11	16.5
18	20	120	90	50	6	18
19	20	120	60	50	11	33

\* The cooling rate at the growth front  $C_{exp}$  ( $^\circ\text{C.min}^{-1}$ ) is simply given by  $C_{exp} = G_{exp} \times V_p$

### 2.2 Films of different thicknesses and subjected to the same thermal gradient process.

Optical profilometry, POM, XRR, and sXRD have been combined to assess thickness, roughness and crystalline morphology of the thin films prepared using different concentrations. The spin-coated thin film **1** at a very low concentration was pretty homogeneous; but the thin films became more and more inhomogeneous with aggregation of small crystals for samples **2-5**, as shown in Figure **3a**, **3c** and Figure **S3** (3D views). Likely, increasing inhomogeneities result from heterogeneous type dewetting which may occur during spin-coating.<sup>37,49</sup> It is known that dust particles can serve as nucleation points in heterogeneous dewetting by weakening mechanically thin films, locally. The DSC curves shown in Figure **2b** suggest that some dust particles are presented in the C8-BTBT-C8 powder sample, result of a ratio of  $T_{LC-Cr} / T_{Cr-LC} = 0.96$  (367.15 K / 382.05 K). A decrease of this ratio close or below 0.8 usually indicates that contamination is significantly reduced.<sup>50</sup> Moreover, the number of dust particles scales with volume.<sup>50</sup> Consequently, for a given sample area, there should be less dust particles in thinner films than in thicker ones, making thicker films more prone to heterogeneous dewetting. Figure **3e** shows that the surface roughness values (*Ra* in nm) of films **1-5** increases non-linearly with concentrations. Only films **1** and **2** showed Kiessig fringes in their XRR curves (Figure **4a**), allowing to determine a thickness of 13.3 and 26.3 nm, respectively.

We now turn our attention to thin films **6-10**, subjected to  $\nabla T$  treatments, which differ by their thickness, see Table 1. They were analysed by POM, optical profilometer, XRR and sXRD. Figure **3b**, **3d** and Figure **S3** show that films **6-8** exhibit a dendritic growth pattern and a partial coverage of glass substrates. But for the film **9**, the dendritic growth is avoided to some degree. However, the continuity of this thin film is still poor. A rather uniform surface morphology has been obtained for film **10**. The dendritic growth was avoided, and the thin film covered the whole area of the substrate, although there were still some small pin-hole-like defects in the sample. As shown in Figure **3e** and Table **S2**, the  $\nabla T$  treatment leads to a little increase of *Ra* values,

in the 6.5 to 15.6 nm range, for films **6-9**. But, for film **10**, the surface roughness decreases, *i.e.* Ra 23.07 nm (before  $\nabla T$ ) versus Ra 5.44 nm (after  $\nabla T$ ). Films **6-9**, give rise to distinctive XRR curves with Kiessig fringes, as displayed in Figure **4b**, allowing the determination of their thicknesses. The thickness scales linearly with concentration as can be seen in Figure **4c** and Table **S2**. However, no prominent Kiessig fringes can be observed for film **10**, because the thickness of the film is too large, resulting in the period of the oscillation is too small for the resolution of our X-ray optics. A noticeable observation in Figure **4c** is that the thickness of the film **1** vs **6** and of the film **2** vs **7** apparently increases. This peculiarity likely results from the discontinuity of thin films **6-7** after  $\nabla T$  processing. Actually, the current results corroborate our previous reports on the annealing of spin-coated C8-BTBT-C8 thin films, without  $\nabla T$  processing, but for which a disordered-layers-to-ordered-islands transition was observed.<sup>38</sup>  
<sup>51</sup> An intense diffraction peak is present at  $q_z$  around  $2.2 \text{ nm}^{-1}$  in all films (Figure **4a** and **4b**). The peak is identified as the 001 Bragg peak of the crystal structure of C8-BTBT-C8 (Figure **S6**). This, combined to the solely observation of  $00l$  family within the whole specular scans of samples (see Figure **S7**), suggests a preferential orientation of the  $(00l)$  planes parallel to the glass substrate for all films, in agreement with previous reports.<sup>52</sup> The

*s*XRD data also highlight a decrease of the FWHM (Figure **S8**, Figure **4d**, and Table **S2**) of the 002 Bragg peak, which is attributed to the increasing of the vertical crystallite size (Figure **4e**, Table **S2**) after the  $\nabla T$  treatment, for all concentrations. The FWHM of the (002) reflection has been used for the analysis because the impact of the Fresnel reflectivity for (002) is less pronounced than that for (001). Altogether, these results suggest a better out-of-plane crystalline order of the thin films after the  $\nabla T$  treatment. The results of the in-plane GIXD of films **5** and **10** are displayed in Figure **S9**. Random in-plane alignment of crystallites was revealed for film **5**, as shown by the presence of all observable  $hk0$  reflections in the  $5\text{-}50^\circ 2\theta_\chi$  range. The in-plane  $2\theta_\chi/\phi$  scan of film **10** presents intense  $\{020\}$  reflections until the second order, highlighting an in-plane alignment. However, a 200 reflection is still observed, although with very small intensity. This can be attributed to the multiple in-plane alignments of the sample. The observation demonstrates that the in-plane crystalline alignment of the thin film is dramatically improved by the  $\nabla T$  approach. All results presented above indicate that the optimal concentration of the C8-BTBT-C8 solution is  $20 \text{ mg.ml}^{-1}$  to produce continuous, uniform and low roughness thin films on glass substrates by the  $\nabla T$  approach.

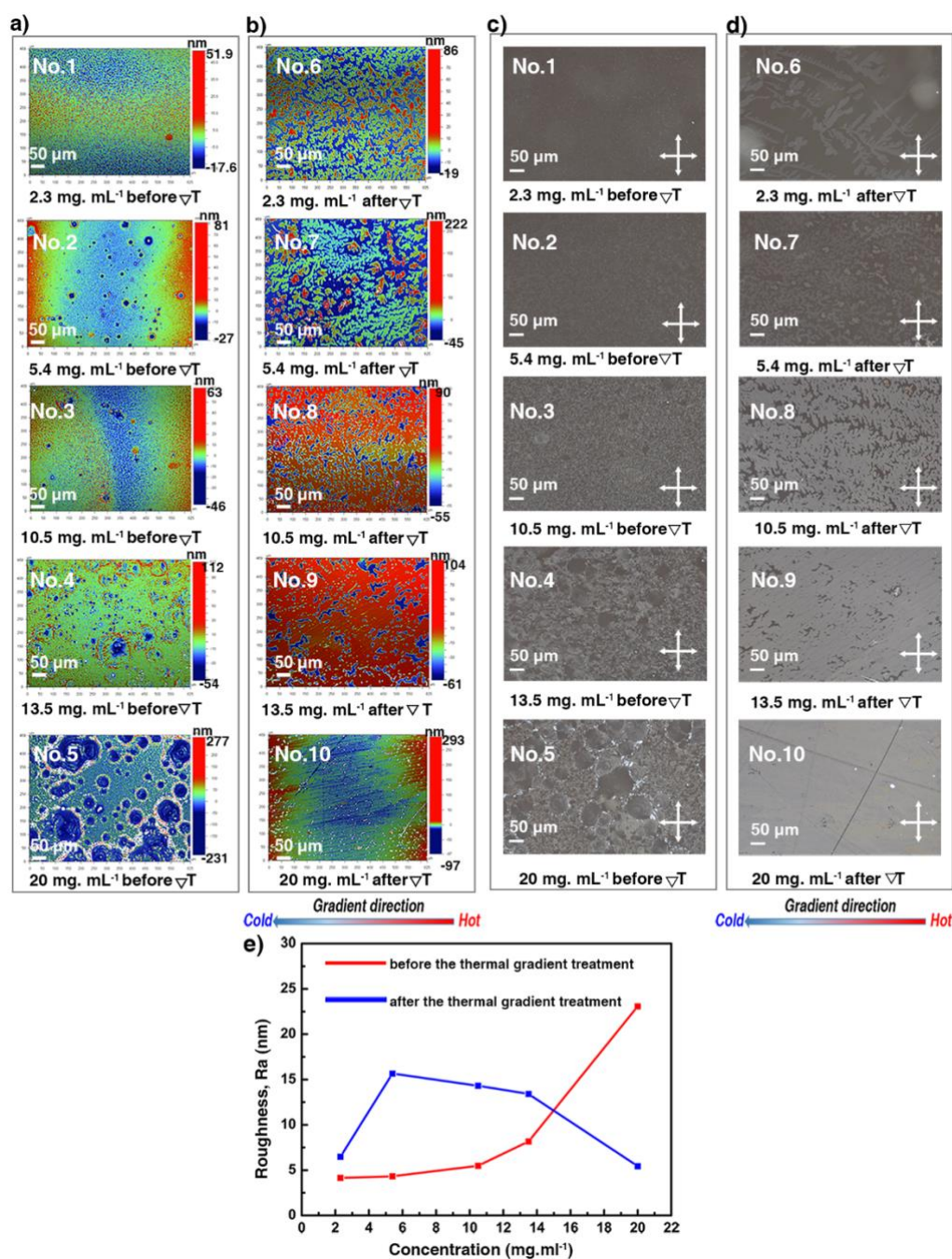


**Fig. 3** Surface morphology of the C8-BTBT-C8 spin-coated thin films produced using different solution concentrations before: a) optical profilometry images and c) POM images; and after the  $\nabla T$  treatment; b) optical profilometry images and d) POM images, recorded at room temperature. The gradient direction is highlighted (bottom). e) Evolution of the film surface roughness (Ra) as a function of the solution concentration. See also Table S2.

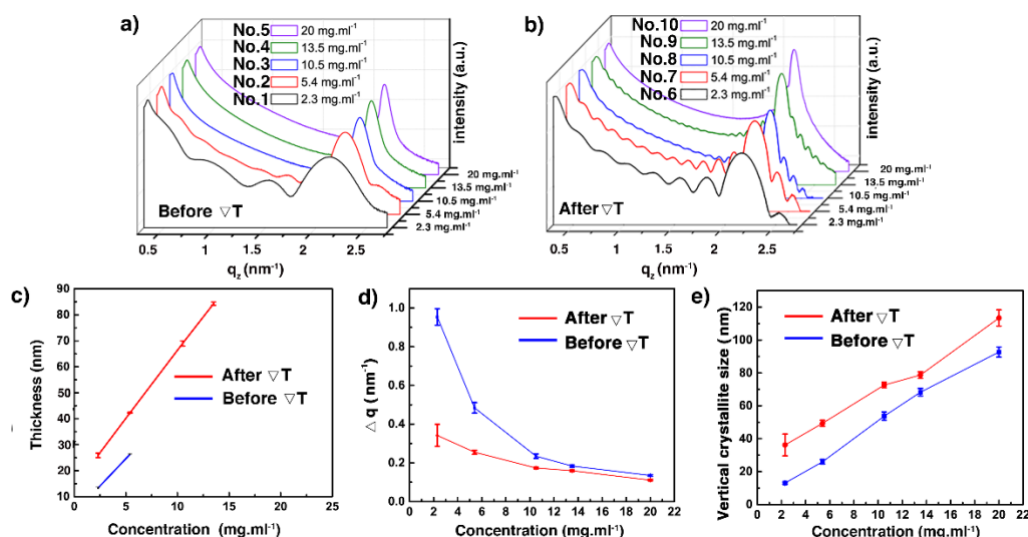


**Fig. 4** XRR curves of the C8-BTBT-C8 thin films (1-10) before (a) and after (b) the  $\nabla T$  treatment, recorded at room temperature. Evolution of the film thicknesses (c), the FWHM of the (002) Bragg peaks (d), and the vertical crystallite size (e) as a function of the solution concentrations before and after the  $\nabla T$  treatments. See also Table S2.

### 2.3 Thin films of C8-BTBT-C8 with comparable thickness but treated by different $\nabla T$ conditions.

Thin films 10-19, obtained at  $20 \text{ mg.ml}^{-1}$ , have been selected to investigate the influence of the  $\nabla T$  conditions on thickness, roughness, and crystalline morphology of the thin films. The investigated  $\nabla T$  conditions are listed in Table 1. After the  $\nabla T$  treatments, roughness and surface morphology were analysed by POM and optical profilometer. The dendritic growth patterns and the partial covering of the substrate, previously observed for thin films produced using lower solution concentrations, appear for the films 11-16, treated by lower pulling rates/cooling rates ( $V_p \leq 10 \text{ }\mu\text{m.s}^{-1}$ ,  $C_{\text{exp}} \leq 6.41 \text{ }^\circ\text{C.min}^{-1}$ ). However, films 10, 17, 18, and 19 cover almost completely the substrates and present large apparently uniform domains. The surface morphology of films 14 and 19 is depicted in Figure 5a and 5b, highlighting the features of partial or complete covering of the glass substrate. The complete set of POM and optical profilometer pictures of films 10-19 is presented in the supporting information, see Figure S4 and S5. As shown in Figure 5c and Table S3, Ra values of films 10-19 decrease by a factor of five to reach a minimum value of about 5 nm. Many small cracks are found in films 10-19, which were generated upon cooling from  $T_c$  to room temperature. They are believed to originate from the difference in the thermal expansion coefficients of C8-BTBT-C8 and the rigid substrate. Figure S11a displays the XRR curves of films 10-19. Although the  $\nabla T$  treatments flatten the film surface and make the films better covering of the substrate, the thicknesses of the films prepared at  $20 \text{ mg.ml}^{-1}$  are too large, causing the oscillation period to approach the limit of our X-ray instrument resolution. Only films 11-14 and 16 show observable Kiessig fringes before  $q_z = 1.7 \text{ nm}^{-1}$ , allowing to evaluate the thicknesses roughly are  $> 130 \text{ nm}$  (Figure S11b, see also in Table S3).

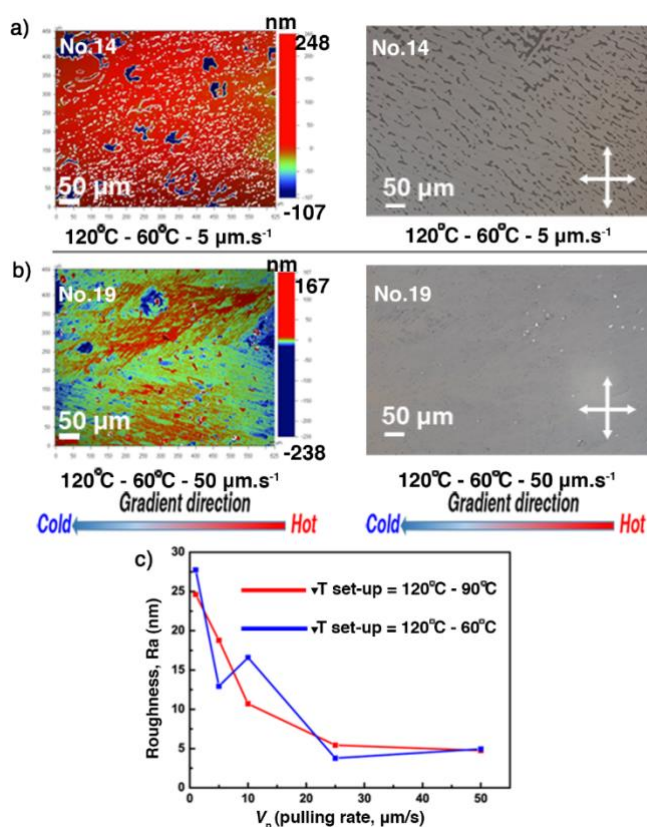


**Fig. 5** The surface morphology (optical profilometry and POM images) of the C8-BTBT-C8 thin films 14 (a) and 19 (b) presents the features of partial or complete covering of the glass substrate. Pictures were recorded at room temperature. The gradient direction is highlighted (bottom). (c) Evolution of the film surface roughness (Ra) as a function of the pulling rate ( $V_p$ ) for different  $T_h - T_c$  couples. See also Table S3.

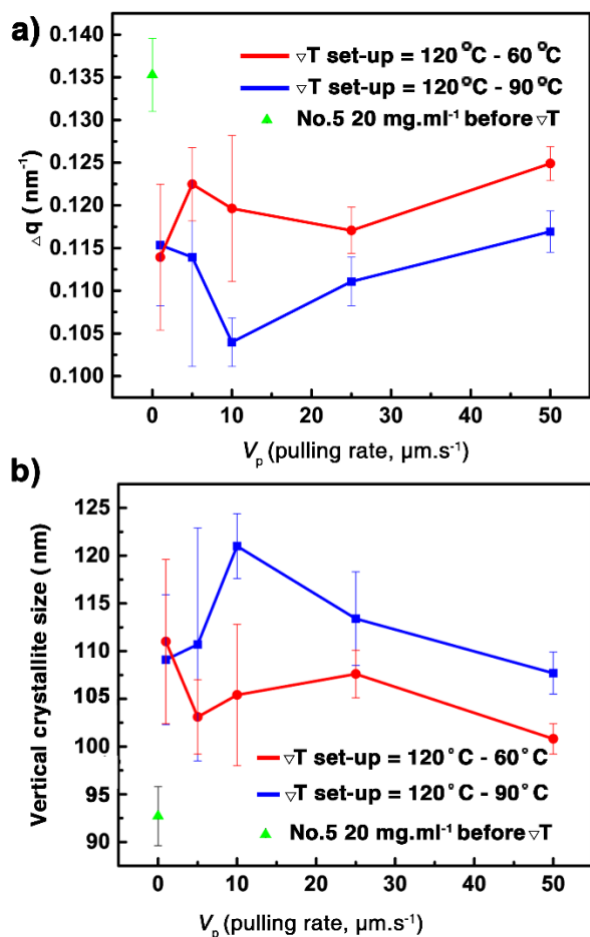


Fig. 6 Evolution of the FWHM of the (002) Bragg peaks of the samples (a) and the vertical crystallite size of films 10–19 as a function of the pulling rate ( $V_p$ ) for two  $T_h - T_c$  couples (b). The data of just coated film 5 are shown for comparison. See also in Table S3.

Similarly to the samples prepared from different concentrations, the observation of a strong diffraction peak at  $q_z$  around  $2.2 \text{ nm}^{-1}$  combined to the solely observation of  $00l$  family through the whole specular diffraction pattern for films 10–19 (see Figure S10) highlights a preferential orientation of the  $(00l)$  planes parallel to the glass substrate. Besides, compared with the just coated film 5, the FWHM of the (002) reflection of films 11–19 is reduced (Figure 6a and Figure S12), resulting from the increasing of the vertical crystallite size after the  $\nabla T$  treatments (Figure 6b). The results highlight again the  $\nabla T$  approach can improve the out-of-plane crystalline order of the thin films. But there is no remarkable difference of the FWHM among films 11–19 (Table S3) due to the limit of the resolution of the X-ray optics. To assess the in-plane alignment of crystallites in the samples, pole figure measurements were carried out for films 10–19 and for film 5, which has undergone no  $\nabla T$  processing (Figure 7 and Figure S14). The particular  $\{113\}$  reflection was chosen because of its high peak intensity (Figure S6). As expected, a totally random in-plane alignment of crystallites was observed for the coated film 5, as evidenced by a wide intensity distribution of the  $\{113\}$  reflection along with azimuthal and meridional rotations of the sample (Figure 7a). This result is consistent with the presence of 110, 020, 120, 200,

130, and 040 peaks in-plane  $2\theta_x/\phi$  scan of film 5, displayed in Figure S9. Importantly, the  $\nabla T$  processing on films 10–19 causes a much better in-plane alignment of crystallites, as shown in Figure 7b–7d and Figure S13. Among films 10, 17, 18, and 19 with good continuity and low surface roughness, number 10 exhibits the best in-plane alignment of crystallites with the narrowest discrete spots, suggesting that highly aligned crystalline domains were produced using  $V_p = 25 \mu\text{m}\cdot\text{s}^{-1}$ ,  $G_{exp} = 6 \text{ }^\circ\text{C}\cdot\text{mm}^{-1}$ , and  $C_{exp} = 9 \text{ }^\circ\text{C}\cdot\text{min}^{-1}$ . However, the uniaxial alignment that takes place exhibit various angles regarding the  $\nabla T$  direction. Films 10–19 are definitely polycrystalline even if large domains are observed. This observation agrees with the POM images in Figures 5 and Figure S4. The lack of univocal uniaxial alignment contrasts with the one observed for terthiophene and resorcinol processed in comparable  $\nabla T$  conditions.<sup>27,30</sup> The reason is likely related to the  $a$  and  $b$  parameters that differ only slightly and to the plate-like crystal morphology, shown in Figure 2a, which results from rather comparable crystal growth rate of planes  $hk0$ . Noteworthy is also that the thermal conductivity coefficients along  $a$  and  $b$  are the same.<sup>48</sup>

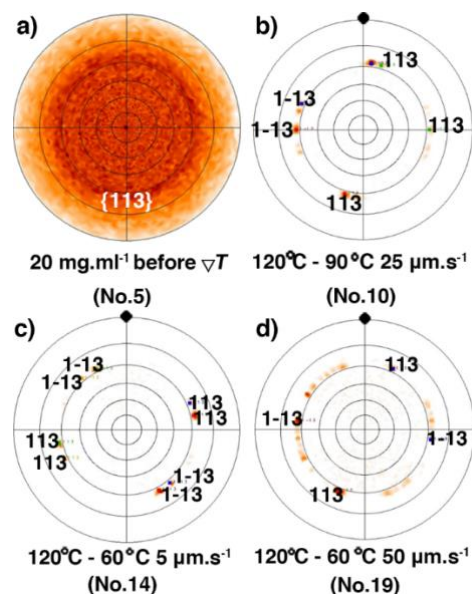


Fig.7 (a) Pole figure of  $\{113\}$  reflections for the spin-coated film 5 before the  $\nabla T$  treatment. Pole-figure measurements of  $\{113\}$  reflection for films 10 (b), 14 (c) and 19 (d), after the  $\nabla T$  treatments. The black solid dot highlights the temperature gradient direction.

## Conclusions

In this contribution, we have explored the post-deposition processing of thin films of C8-BTBT-C8 compound by directional crystallization using a temperature gradient. The smectic phase of C8-BTBT-C8 prevents dewetting and allows to decouple film formation by spin-coating from the control of the crystalline morphology. Results obtained by POM, optical profilometer, XRR,  $s$ XRD, GIXD and pole figures put forward a dramatic effect of the temperature gradient processing. Roughness drops and films flatten significantly. They cover much better the substrate. Considerably larger and more

ordered crystal domains are obtained. However, no univocal uniaxial alignment is observed. This study demonstrates also that directional crystallization is achievable using a liquid crystal to crystal phase transition.

### Conflicts of interest

There are no conflicts to declare.

### Acknowledgements

G.L. thanks the European Union's Horizon 2020 Research and Innovation Program under the Marie Skłodowska-Curie grant agreement n°. 791207 (PARADA) and postdoctoral fellowship support from the FNRS for the POLYMOL project n° 1.B.253.20F. YG is thankful to the Belgian National Fund for Scientific Research (FNRS) for financial support through research projects BTBT n° 2.4565.11, Phasetrans n° T.0058.14, Pi-Fast n° T.0072.18, and 2D to 3D No. 30489208. Financial supports from the French Community of Belgian (ARC n° 20061) and by the Walloon Region (WCS No. 1117306, SOLIDYE n° 1510602) are also acknowledged. G.S. acknowledges postdoctoral fellowship support from the FNRS.

### Notes and references

- J. H. Burroughes, D. D. C. Bradley, A. R. Brown, R. N. Marks, K. Mackay, R. H. Friend, P. L. Burns and A. B. Holmes, Light-emitting diodes based on conjugated polymers, *Nature*, 1990, **347**, 539-541.
- Z. Bao and J. Locklin, *Organic Field-Effect Transistors*, CRC Press, Inc.: 2007.
- H. Uoyama, K. Goushi, K. Shizu, H. Nomura and C. Adachi, Highly efficient organic light-emitting diodes from delayed fluorescence, *Nature*, 2012, **492**, 234-238.
- G. Schweicher, G. Garbay, R. Jouclas, F. Vibert, F. Devaux and Y. H. Geerts, Molecular Semiconductors for Logic Operations: Dead-End or Bright Future?, *Adv. Mater*, 2020, **32**, 1905909.
- J. Zaumseil and H. Sirringhaus, Electron and Ambipolar Transport in Organic Field-Effect Transistors, *Chem. Rev*, 2007, **107**, 1296-1323.
- P. J. Skabara, J.-B. Arlin and Y. H. Geerts, Close Encounters of the 3D Kind – Exploiting High Dimensionality in Molecular Semiconductors, *Adv. Mater*, 2013, **25**, 1948-1954.
- S. Sergeev, W. Pisula and Geerts, Y. H., Discotic liquid crystals: a new generation of organic semiconductors, *Chem. Soc. Rev*, 2007, **36**, 1902-1929.
- J. Rivnay, S. C. B. Mannsfeld, C. E. Miller, A. Salleo and M. F. Toney, Quantitative Determination of Organic Semiconductor Microstructure from the Molecular to Device Scale, *Chem. Rev.*, 2012, **112**, 5488-5519.
- A. Salleo, R. J. Kline, D. M. DeLongchamp and M. L. Chabiny, Microstructural Characterization and Charge Transport in Thin Films of Conjugated Polymers, *Adv. Mater* 2010, **22**, 3812-3838.
- D. M. DeLongchamp, R. J. Kline, D. A. Fischer, L. J. Richter, and M. F. Toney, Molecular Characterization of Organic Electronic Films, *Adv. Mater*, 2011, **23**, 319-337.
- Y. Diao, L. Shaw, Z. Bao and S. C. B. Mannsfeld, Morphology control strategies for solution-processed organic semiconductor thin films, *Energy Environ. Sci.* 2014, **7**, 2145-2159.
- H. Li, G. Giri, J. B. H. Tok and Z. Bao, Toward high-mobility organic field-effect transistors: Control of molecular packing and large-area fabrication of single-crystal-based devices, *MRS Bulletin*, 2013, **38**, 34-42.
- A. A. Virkar, S. Mannsfeld, Z. Bao and N. Stingelin, Organic Semiconductor Growth and Morphology Considerations for Organic Thin-Film Transistors, *Adv. Mater* 2010, **22**, 3857-3875.
- S. Liu, W. M. Wang, A. L. Briseno, S. C. B. Mannsfeld and Z. Bao, Controlled Deposition of Crystalline Organic Semiconductors for Field-Effect-Transistor Applications, *Adv. Mater* 2009, **21**, 1217-1232.
- Y. Wen, Y. Liu, Y. Guo, G. Yu and W. Hu, Experimental Techniques for the Fabrication and Characterization of Organic Thin Films for Field-Effect Transistors, *Chem. Rev.* 2011, **111**, 3358-3406.
- C. Park, J. E. Park, H. C. Choi, Crystallization-Induced Properties from Morphology-Controlled Organic Crystals, *Acc. Chem. Res.* 2014, **47**, 2353-2364.
- H. Minemawari, T. Yamada, H. Matsui, J. Y. Tsutsumi, S. Haas, R. Chiba, R. Kumai and T. Hasegawa, Inkjet printing of single-crystal films, *Nature*, 2011, **475**, 364-367.
- W. Pisula, A. Menon, M. Stepputat, I. Lieberwirth, U. Kolb, A. Tracz, H. Sirringhaus, T. Pakula and K. Müllen, A Zone-Casting Technique for Device Fabrication of Field-Effect Transistors Based on Discotic Hexa-peri-hexabenzocoronene, *Adv. Mater.* 2005, **17**, 684-689.
- G. Giri, E. Verploegen, S. C. B. Mannsfeld, S. Atahan-Evrenk, D. H. Kim, S. Y. Lee, H. A. Becerril, A. Aspuru-Guzik, M. F. Toney and Z. Bao, Tuning charge transport in solution-sheared organic semiconductors using lattice strain, *Nature* 2011, **480**, 504-508.
- D. T. James, J. M. Frost, J. Wade, J. Nelson and J.-S. Kim, Controlling Microstructure of Pentacene Derivatives by Solution Processing: Impact of Structural Anisotropy on Optoelectronic Properties, *ACS Nano* 2013, **7**, 7983-7991.
- Y. Diao, B. C. K. Tee, G. Giri, J. Xu, D. H. Kim, H. A. Becerril, R. M. Stoltenberg, T. H. Lee, G. Xue, S. C. B. Mannsfeld and Z. Bao, Solution coating of large-area organic semiconductor thin films with aligned single-crystalline domains, *Nature Mater*, 2013, **12**, 665-671.
- A. Yamamura, S. Watanabe, M. Uno, M. Mitani, C. Mitsui, J. Tsurumi, N. Isahaya, Y. Kanaoka, T. Okamoto and J. Takeya, Wafer-scale, layer-controlled organic single crystals for high-speed circuit operation, *Sci. Adv.* 2018, **4**: eaao5758.
- J. C. Maunoury, J. R. Howse and M. L. Turner, Melt-Processing of Conjugated Liquid Crystals: A Simple Route to Fabricate OFETs, *Adv. Mater*, 2007, **19**, 805-809.
- J.-C. Ribierre, Z. Li, X. Liu, E. Lacaze, B. Heinrich, S. Méry, P. Sleczkowski, Y. Xiao, F. Lafolet, D. Hashizume, T. Aoyama, M. Uchiyama, J. W. Wu, E. Zaborova, F. Fages, A. D'Aléo, F. Mathevet and C. Adachi, A solvent-free and vacuum-free melt-processing method to fabricate organic semiconducting layers with large crystal size for organic electronic applications, *J. Mater. Chem. C* 2019, **7**, 3190-3198.
- A. Kim, K.-S. Jang, J. Kim, J. C. Won, M. H. Yi, H. Kim, D. K. Yoon, T. J. Shin, M.-H. Lee, J.-W. Ka and Y. H. Kim, Solvent-Free Directed Patterning of a Highly Ordered Liquid Crystalline Organic Semiconductor via Template-Assisted Self-Assembly for Organic Transistors, *Adv. Mater* 2013, **25**, 6219-6225.
- I. Fujieda, N. Iizuka and Y. Onishi, Directional solidification of C8-BTBT films induced by temperature gradients and its application for transistors, *Proc. SPIE*: 2015, **9360**, 936012.

- 27 G. Schweicher, N. Paquay, C. Amato, R. Resel, M. Koini, S. Talvy, V. Lemaury, J. Cornil, Y. Geerts and G. Gbabode, Toward Single Crystal Thin Films of Terthiophene by Directional Crystallization Using a Thermal Gradient, *Cryst. Growth Des* 2011, **11**, 3663-3672.
- 28 B. Chattopadhyay, L. Jacobs, P. Panini, I. Salzmänn, R. Resel and Y. Geerts, Accessing Phase-Pure and Stable Acetaminophen Polymorphs by Thermal Gradient Crystallization, *Cryst. Growth Des* 2018, **18**, 1272-1277.
- 29 R. Resel, A. O. F. Jones, G. Schweicher, R. Fischer, N. Demitri and Y. H. Geerts, Polymorphism of terthiophene with surface confinement, *IUCrJ* 2018, **5**, 304-308.
- 30 P. Panini, B. Chattopadhyay, O. Werzer and Y. Geerts, Crystal Growth Alignment of  $\beta$ -Polymorph of Resorcinol in Thermal Gradient, *Cryst. Growth Des* 2018, **18**, 2681-2689.
- 31 K. A. Jackson, *Kinetic Processes: Crystal Growth, Diffusion, and Phase Transitions in Materials.*, Wiley: 2010.
- 32 T. Asano, Melt-crystallization of n-alkanes and polyethylene in a temperature gradient, *Polym. Bull.* 1983, **10**, 547-552.
- 33 T. Asano, Melt-crystallization of n-alkanes and polyethylene in a temperature gradient, *Polym. Bull.* 1984, **12**, 543-546.
- 34 T. Asano, M. F. Mina, A. Nishida, S. Yoshida and Y. Fujiwara, Crystallization of a low molecular weight polyethylene and paraffins under a temperature gradient, *J. Macromol. Sci. B*, 2001, **40**, 355-367.
- 35 J. L. Stevenson, Growth and characterisation of single crystal optical fibre waveguides - meta-nitroaniline, *J. Cryst. Growth*, 1977, **37**, 116-128.
- 36 H. Murayama, K. Muta and H. Matsuura, Control of crystal orientation in an organic-crystal-cored fibre, *J. Phys. D: Appl. Phys.* 1993, **26**, B248-B251.
- 37 O. K. C. A. R. Tsui and P. Thomas, *Polymer Thin Films.*, World Scientific, Singapore, 2008.
- 38 M. Dohr, H. M. A. Ehmann, A. O. F. Jones, I. Salzmänn, Q. Shen, C. Teichert, C. Ruzié, G. Schweicher, Y. H. Geerts, R. Resel, M. Sferrazza and O. Werzer, Reversibility of temperature driven discrete layer-by-layer formation of dioctyl-benzothieno-benzothiophene films, *Soft Matter*, 2017, **13**, 2322-2329.
- 39 H. Iino and J.-i. Hanna, Availability of Liquid Crystallinity in Solution Processing for Polycrystalline Thin Films, *Adv. Mater.* 2011, **23**, 1748-1751.
- 40 H. Ebata, T. Izawa, E. Miyazaki, K. Takimiya, M. Ikeda, H. Kuwabara and T. Yui, Highly Soluble [1]Benzothieno[3,2-b]benzothiophene (BTBT) Derivatives for High-Performance, Solution-Processed Organic Field-Effect Transistors, *J. Am. Chem. Soc.* 2007, **129**, 15732-15733.
- 41 T. Izawa, E. Miyazaki and K. Takimiya, Molecular Ordering of High-Performance Soluble Molecular Semiconductors and Re-evaluation of Their Field-Effect Transistor Characteristics, *Adv. Mater* 2008, **20**, 3388-3392.
- 42 C. Grigoriadis, C. Niebel, C. Ruzié, Y. H. Geerts and G. Floudas, Viscoelastic, and Dielectric Properties of Symmetric and Asymmetric Alkyl[1]benzothieno[3,2-b][1]benzothiophenes, *J. Phys. Chem. B* 2014, **118**, 1443-1451.
- 43 B. E. Warren, *X-Ray Diffraction*. Addison-Wesley, Reading, MA, 1969.
- 44 I. Salzmänn, R. Resel, software for the analysis of X-ray diffraction pole figures with IDL, *J. Appl. Crystallogr.* 2004, **37**, 1029-1033.
- 45 A. Bravais, *Etudes Cristallographiques*. Gauthier-Villars: 1866.
- 46 G. Friede, Crystal Morphologies, *Bull. Soc. Franc. Mineral.*, 1907, **30**, 326-455.
- 47 J. D. H. Donnay and D. Harker, A new law of crystal morphology extending the law of Bravais, *Am. Mineral.*, 1937, **22**, 446-467.
- 48 W. Shi, J. Chen, J. Xi, D. Wang and Z. Shuai, Search for Organic Thermoelectric Materials with High Mobility: The Case of 2,7-Dialkyl[1]benzothieno[3,2-b][1]benzothiophene Derivatives, *Chem. Mater* 2014, **26**, 2669-2677.
- 49 R. Konnur, K. Kargupta and A. Sharma, , Instability and Morphology of Thin Liquid Films on Chemically Heterogeneous Substrates, *Phys. Rev. Lett.* 2000, **84**, 931-934.
- 50 K. A. Jackson, Nucleation from the Melt, *Ind. Eng. Chem.*, 1965, **57**, 29-32.
- 51 M. Dohr, O. Werzer, Q. Shen, I. Salzmänn, C. Teichert, C. Ruzié, G. Schweicher, Y. H. Geerts, M. Sferrazza and R. Resel, Dynamics of Monolayer-Island Transitions in 2,7-Dioctyl-benzothienobenzothiophene Thin Films, *ChemPhysChem* 2013, **14**, 2554-2559.
- 52 G. Gbabode, M. Dohr, C. Niebel, J.-Y. Balandier, C. Ruzié, P. Négrier, D. Mondieig, Y. H. Geerts, R. Resel and M. Sferrazza, X-ray Structural Investigation of Nonsymmetrically and Symmetrically Alkylated [1]Benzothieno[3,2-b]benzothiophene Derivatives in Bulk and Thin Films, *ACS Appl. Mater. Interfaces* 2014, **6**, 13413-13421.